

Article

Fabrication, Performance, Characterization and Experimental Calibration of Embedded Thin-Film Sensor for Tool Cutting Force Measurement

Yunping Cheng, Wenge Wu *, Lijuan Liu, Yuntao Zhang, Zhenyu He and Ding Song

School of Mechanical Engineering, North University of China, Taiyuan 030051, China; ypchengbk@163.com (Y.C.); liulijuan@nuc.edu.cn (L.L.); zyt7262@126.com (Y.Z.); hezhenyu0229@163.com (Z.H.); sd199402@163.com (D.S.)

* Correspondence: wuwenge@nuc.edu.cn; Tel.: +86-137-5488-1640

Abstract: Thin-film strain sensors are widely used because of their small volume, fast strain response and high measurement accuracy. Among them, the thin-film material and preparation process of thin-film strain sensors for force measurement are important aspects. In this paper, the preparation process parameters of the transition layer, insulating layer and Ni-Cr alloy layer in a thin-film strain sensor are analyzed and optimized, and the influence of each process parameter on the properties of the thin film are discussed. The surface microstructure of the insulating layer with Al₂O₃ or Si₃N₄ transition layers and the film without transition layer were observed by atomic force microscopy. It is analyzed that adding a transition layer between the stainless steel substrate and insulation layer can improve the adhesion and flatness of the insulation layer. The effects of process parameters on elastic modulus, nanohardness and strain sensitivity coefficient of the Ni-Cr resistance layer are discussed, and electrical parameters such as the resistance strain coefficient are analyzed and characterized. The static calibration of the thin-film strain sensor is carried out, and the relationship between the strain value and the output voltage is obtained. The results show that the thin-film strain sensor can obtain the strain generated by the cutting tool and transform it into an electrical signal with good linearity through the bridge, accurately measuring the cutting force.

Keywords: thin-film strain sensor; cutting force; preparation process; performance characterization



Citation: Cheng, Y.; Wu, W.; Liu, L.; Zhang, Y.; He, Z.; Song, D. Fabrication, Performance, Characterization and Experimental Calibration of Embedded Thin-Film Sensor for Tool Cutting Force Measurement. *Micromachines* **2022**, *13*, 310. <https://doi.org/10.3390/mi13020310>

Academic Editor: Niall Tait

Received: 11 January 2022

Accepted: 12 February 2022

Published: 17 February 2022

Publisher's Note: MDPI stays neutral with regard to jurisdictional claims in published maps and institutional affiliations.



Copyright: © 2022 by the authors. Licensee MDPI, Basel, Switzerland. This article is an open access article distributed under the terms and conditions of the Creative Commons Attribution (CC BY) license (<https://creativecommons.org/licenses/by/4.0/>).

1. Introduction

The cutting force directly affects the quality of the work-piece and tool life as one of important parameters in metal cutting processes. Accurate real-time monitoring of cutting force is helpful to study the mechanism of the cutting process and effectively control machining quality and tool life. Therefore, many researchers have done a lot of work on cutting force [1–6]. Cutting force dynamometers include strain dynamometers, piezoelectric dynamometers, current dynamometers, capacitive and hydraulic dynamometers. Among them, the strain dynamometer and piezoelectric dynamometer are the main dynamometers used. The piezoelectric dynamometer measures the cutting force through the piezoelectric effect of piezoelectric crystals [7,8]. The strain dynamometer measures the cutting force through the strain effect [9].

In recent years, with the rapid development of microelectromechanical systems (MEMS), thin-film deposition and microelectro mechanical system technology have been developed rapidly. The thin-film strain sensor is one of the kinds of dynamometer which can monitor the cutting process in real time [10,11]. The material and quality are important to the performance of strain sensors. As a result, some scholars have studied various functional layers. For the transition layer film, Zhang et al. studied a series of TiN films with different N/Ti ratios and phase evolution and mechanical properties of TiN films [12]. The hardness of the film increases with the increase of the chemometric ratio to the TiN phase, while the resistance to plastic deformation ratio of H^3/E^2 (H : hardness/ E : elastic modulus)

as an index of the toughness decreases [12]. Chen et al. deposited TiN films on 304 stainless steel surfaces by multi-arc ion plating and studied their tribology properties in a nitrogen atmosphere with GCr15 steel balls. Results showed that the TiN (200) phase has higher smoothness [13]. Chou et al. used hollow cathode discharge ion plating (HCD-IP) technology to deposit a TiN film on a 304 stainless steel surface. Hardness values ranged from 14.9 to 33.6 GPa and increased with increasing film thickness. The stacking factor of TiN film is 0.62–0.99, which increases with the increase of film thickness [14]. Qi et al. prepared nitrogen-doped titanium thin-films by direct current reactive magnetron sputtering and added different proportions of nitrogen doping into argon. Nitrogen atom energy densely arrayed hexagonal (hcp) α -Ti phase is transformed into Ti crystal (100) and Ti (002) is oriented to face-centered cubic (fcc) TiN phase. An appropriate partial pressure of nitrogen can effectively reduce the roughness and control the internal stress [15].

For insulating film, Kishore Kumar et al. used reactive RF magnetron sputtering technology to deposit Si₃N₄ films on surface-treated and untreated aluminum alloy substrates, observing that the lattice strain of the film decreases with the increase of grain size [16]. Nemanič et al. used reactive RF magnetron sputtering to deposit 500 and 700 nm thick amorphous Si₃N₄ films on an Eurofer substrate [17]. Batan et al. used reactive DC magnetron sputtering to prepare Si₃N₄ films on stainless steel substrates, preliminarily studied the influence of nitrogen pressure on chemical composition, microstructure and purity [18]. Yao et al. deposited silicon nitride films on silicon (100) and 316L stainless steel substrates by pulse reactive closed unbalanced magnetron sputtering. They studied the influence of the N₂ component on its chemical composition, tribology and wetting behavior [19].

Petley et al. deposited Ni-Cr alloy thin-films as the sensitive layer film at room temperature using magnetron co-sputtering technology and found that when it contained 80% Ni with 20% Cr it showed the most obvious columnar structure, had the highest resistivity, indentation hardness and elastic modulus, and good mechanical and electrical properties [20]. Lai et al. deposited Ni₈₀Cr₂₀ alloy films on copper foil, glass and silicon substrates, respectively, by DC magnetron sputtering. The resistivity of Ni-Cr film deposited on copper foil is higher than that of glass or silicon substrates. However, the resistance temperature coefficient (TCR) of Ni-Cr thin-films is not affected by the different substrates [21]. The deposition parameters such as sputtering power, substrate temperature and argon pressure were optimized by the Taguchi method. The polarity analysis shows that the sputtering power is the most important factor affecting the electrical properties of the nickel-chromium alloy film, and the low temperature resistance coefficient of 374.78 ppm/K is obtained [22].

Thin-film strain sensors is one of new type of microsensors which it can be integrated with tools and avoid direct contact with the workpieces, and interference without the cutting process, while allowing for data acquisition very close to the tip of the tool. This research group has done some research on the measurement of cutting force with embedded thin-film strain sensors, focusing on the measurement mechanism, structure design and preparation process of thin-film strain sensors [23–29].

The materials and quality of the thin-film are important to obtain good strain sensor performance. In this paper, the effect of the material and technology parameters of the membrane system film on the film quality and performance are analyzed, mechanical and electrical performance of the resistor grid layers are discussed, and the sensor strain coefficient is calibrated by experiments. As a result, we can determine the best film materials, optimize the process parameters, improve the performance of the film system and microsensor, and provide technical support for the application of strain film sensors in the measurement of cutting force.

2. Experimental Study of Thin-Film Strain Sensor Preparation

2.1. Preparation Process Flow of Thin-Film Strain Sensor

As shown in Figure 1, the preparation process of thin-film strain sensor mainly includes substrate preparation, sputtering transition layer, sputtering insulating layer, sputtering resistance grid layer, etching resistance grid structure, performance test and packaging.

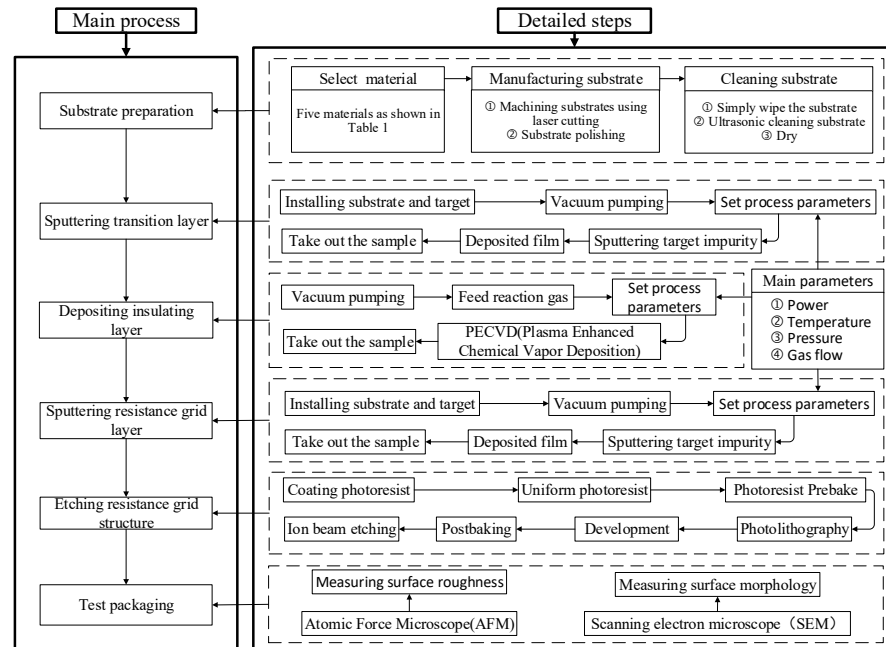


Figure 1. Process flow diagram.

The material of substrate can be selected from among AISI 1045, Ti6Al4V, AISI 304, C2800 brass and Al 1060. The mechanical properties and the macro- and micromorphology of the pretreated parts are shown in Table 1. There is small difference of tiny lines on the macroscopic surface of AISI 1045, Ti6Al4V, C2800 brass, Al 1060. There are many crisscross scratches on surface of AISI 1045 and Ti6Al4V, and scratches on surface of AISI 1045 are deeper. Scratches on surface of C2800 brass and Al 1060 are in the same direction. There are minimal scratches on surface of AISI 304. Stainless steel is often used as a substrate material due to its corrosion resistance, heat resistance and good mechanical elastic behavior [30–32]. Therefore, stainless steel was selected as the substrate material. Table 2 lists the physical properties and application schemes of membrane materials for thin-film strain sensors. Figure 2 shows that the Structure of thin-film strain sensor and resistance grid. When Si_3N_4 is deposited directly on the stainless steel substrate as an insulating layer, cracks will appear. As a result, the transition layer between the insulating layer and the substrate improves the performance of the insulating layer.

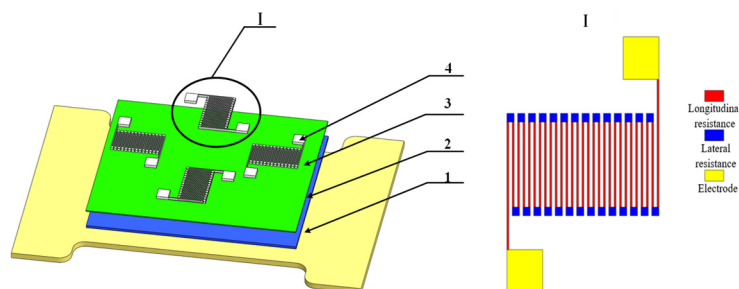


Figure 2. Structure of thin-film strain sensor and resistance grid. 1, Elastic substrate; 2, Transition layer; 3, Insulating layer; 4, Resistance grid layer.

Table 1. Substrate material characteristics, macroscopic features and microscopic features.


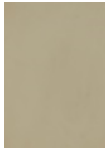



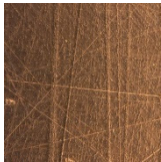

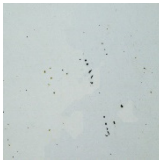

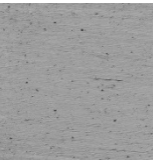
Material	AISI 1045	Ti6Al4V	AISI 304	C2800 Brass	Al 1060
Elastic modulus (GPa)	210	113	200	100	69
Shear modulus (GPa)	79	44	75	37	26
Thermal Expansion Coefficient (10 ⁻⁶ /K)	11.59	7.89	15	18	23.6
Yield strength (MPa)	355	825–895	205	239	135
Poisson’s ratio	0.31	0.34	0.29	0.33	0.33
Material appearance					
Ultra depth of field micrograph (500 times)					

Table 2. Material properties and application of various types of films.

	Al ₂ O ₃ Film	TiN Film	Si ₃ N ₄ Film	Ni ₈₀ Cr ₂₀ Film
Elastic Modulus (GPa)	357	279	304	186
Poisson’s Ratio	0.21–0.27	0.25	0.24	0.38
Thermal Expansion Coefficient (10 ⁻⁶ /K)	7–10.3	7.4	2.45	14
Nano-hardness (GPa)	14.2	33.6	17.6	9.7
Application	Transition layer	Transition layer	Insulating layer	Resistance grid layer

2.2. Preparation and Test Scheme of Membrane System of Thin-Film Strain Sensor

2.2.1. Preparation Process of Si₃N₄ Film

During the preparation of insulating layer Si₃N₄ film, sputtering power, sputtering pressure, gas flow ratio and substrate temperature are the four main deposition process parameters. In the preliminary test, several different values are selected for each process parameter by single factor experiments, and four levels for every process parameter are selected. In order to optimize the process parameters, the four levels of each factor are studied by orthogonal experiments. The level values of the orthogonal factors of the four process parameters are shown in Table 3. The orthogonal experimental design and test results of the four deposition process parameters are shown in Table 4.

Table 3. Level table of orthogonal test factors of Si₃N₄ film.

Level	A	B	C	D
	Sputtering Power (W)	Sputtering Pressure (Pa)	Gas Flow Ratio	Substrate Temperature (°C)
1	60	0.6	0	ambient temperature
2	80	0.8	0.125	100
3	100	1.0	0.2	200
4	120	1.2	0.25	300

Table 4. $L_{16}(4^4)$ Orthogonal test design and results of Si_3N_4 film.

Number	A	B	C	D	Deposition Rate v /(nm/min)	Surface Roughness Ra /(nm)
1	60	0.6	0	20	5.442	48
2	60	0.8	0.125	100	3.080	47
3	60	1.0	0.2	200	3.091	48
4	60	1.2	0.25	300	3.245	49
5	80	0.6	0.125	200	4.031	52
6	80	0.8	0	300	6.052	56
7	80	1.0	0.25	20	3.175	49
8	80	1.2	0.2	100	4.678	51
9	100	0.6	0.2	300	4.579	52
10	100	0.8	0.25	200	5.012	49
11	100	1.0	0	100	8.546	54
12	100	1.2	0.125	20	6.149	45
13	120	0.6	0.25	100	7.125	52
14	120	0.8	0.2	20	8.328	54
15	120	1.0	0.125	300	9.058	56
16	120	1.2	0	200	13.012	59

2.2.2. Preparation Process of Al_2O_3 and TiN Transition Layer Films

Stainless steel 304 is used as the substrate material because of its corrosion resistance, heat resistance and good mechanical elasticity [30–32]. Cracks would appear and spread and eventually the coating could fall off when Si_3N_4 film is directly deposited. In order to increase the adhesion between Si_3N_4 and the substrate, a transition layer need to be added. In this paper, Al_2O_3 and TiN are used as transition layer materials. The thin-film strain sensor can meet the requirements of high strain rate and improve the measurement accuracy and service life of the sensor.

Before depositing the transition layer, the stainless-steel substrate was subjected to surface treatment to obtain a surface roughness of 30–50 nm, which was ultrasonically cleaned with acetone and absolute alcohol for 20 min. sputtering power, sputtering pressure, and Ar: O_2 flow ratio are the main process parameters in the preparation process of Al_2O_3 film. In this experiment, the target spacing is always 30 mm. The change range of sputtering power is 60~100 W, sputtering pressure is 0.5~2.5 Pa, Ar: O_2 flow ratio is 10:1~50:1. The Ar: N_2 flow ratio of nitrogen and argon and the substrate negative bias are the main process parameters in preparing process of TiN film. The range of Ar: N_2 flow ratio is 20:1~60:1, and substrate negative bias is 0~100 V.

2.2.3. The Preparation Process of Ni-Cr Alloy Film

Sputtering power, sputtering pressure, substrate negative bias and substrate temperature are the main process parameters in the preparation process of Ni-Cr alloy films. The relationship between process parameters and the deposition rate of nickel-chromium films is analyzed by orthogonal experiment. The factor level table of the four process parameters is shown in Table 5. The change range of sputtering power is 80~140 W, 20 W intervals between each level, sputtering pressure is 1.0~2.5 Pa, substrate negative bias is 0~150 V, and substrate temperature is 20~300 °C.

Table 5. Level table of orthogonal test factors of Ni-Cr alloy film.

Level	A	B	C	D
	Sputtering Power (W)	Sputtering Pressure (Pa)	Substrate Negative Bias (V)	Substrate Temperature (°C)
1	80	1.0	0	20
2	100	1.5	50	100
3	120	2.0	100	200
4	140	2.5	150	300

Table 6 shows the orthogonal experiment design and test results of deposition rate of Ni-Cr alloy film.

Table 6. $L_{16}(4^4)$ Orthogonal test design and results of Ni-Cr alloy film.

Number	A	B	C	D	Deposition Rate (W)
1	80	1.0	0	20	47.67
2	80	1.5	50	100	49.11
3	80	2.0	100	200	50.89
4	80	2.5	150	300	52.77
5	100	1.0	50	200	56.21
6	100	1.5	0	300	54.26
7	100	2.0	150	20	61.06
8	100	2.5	100	100	58.55
9	120	1.0	100	300	63.85
10	120	1.5	150	200	66.98
11	120	2.0	0	100	61.41
12	120	2.5	50	20	62.69
13	140	1.0	150	100	71.03
14	140	1.5	100	20	69.66
15	140	2.0	50	300	68.21
16	140	2.5	0	200	66.01

The Ni-Cr alloy film is etched into the shape of resistance grid by ion beam etching. After sputtering the transition layer, insulating layer and Ni-Cr film on the substrate, the Ni-Cr alloy film resistance grid is obtained by ion beam etching through photolithography and development. Incident angle, Argon flow and substrate negative bias are main process parameters of ion beam etching. The factor level table of the three process parameters is shown in Table 7.

Table 7. Level table of orthogonal test factors of ion beam etching.

Level	X	Y	Z
	Incident Angle (°)	Argon Flow (m^3/s)	Substrate Negative Bias (V)
1	20	1×10^{-5}	350
2	45	1.25×10^{-5}	450
3	70	1.5×10^{-5}	550

Table 8 shows the orthogonal experiment design and test results of etching rate, surface roughness and resistivity.

Table 8. Ion beam etching orthogonal test design and results.

Number	Incident Angle (°)	Argon Flow (m^3/s)	Substrate Negative Bias (V)	Etching Rate $v/(\text{nm}/\text{min})$		Surface Roughness $R_a/(\text{nm})$	Resistivity $P(\mu\Omega \cdot \text{m})$
				Ni-Cr	Photoresist AZ6140		
1	20	1×10^{-5}	350	19.8	18.2	35	1.21
2	20	1.25×10^{-5}	450	25.0	23.4	38	1.57
3	20	1.5×10^{-5}	550	31.5	27.8	41	1.68
4	45	1×10^{-5}	450	23.6	22.6	31	1.10
5	45	1.25×10^{-5}	550	29.1	26.3	33	1.19
6	45	1.5×10^{-5}	350	20.9	18.1	28	1.06
7	70	1×10^{-5}	550	27.6	26.6	37	1.46
8	70	1.25×10^{-5}	350	20.2	17.4	32	1.16
9	70	1.5×10^{-5}	450	26.1	24.2	36	1.32

2.3. Result Analysis

2.3.1. Variance Analysis of Orthogonal Test of Process Parameters for Si_3N_4 Film

Table 9 is the result of variance analysis according to the orthogonal test results of Table 4 which the orthogonal experimental design and test results of the four deposition process parameters of Si_3N_4 film.

Table 9. Variance analysis of film deposition rate test results of Si₃N₄ film.

	Degree of Freedom	Deviation Square Sum	Mean Deviation Squares Sum	F Ratio
A: Sputtering power/(W)	3	75.706	25.235	142.571
B: Sputtering pressure/(Pa)	3	4.837	1.612	9.107
C: Gas flow ratio	3	31.234	10.411	58.819
D: Substrate temperature/(°C)	3	0.778	0.259	1.463
Error	3	0.53	0.177	

Comparing the F value of the mean deviation square sum and the mean deviation squares errors of each parameter, the influence degree of the process parameters on deposition rate of the Si₃N₄ film can be obtained as follows: Sputtering power A > Gas flow ratio C > Sputtering pressure B > Substrate temperature D.

It can be seen from Table 10 that the influence degree of the process parameters on surface roughness of the Si₃N₄ film can be obtained as follows: Sputtering power A > Gas flow ratio C > Sputtering pressure B > Substrate temperature D.

Table 10. Variance analysis of film surface roughness Ra test results of Si₃N₄ film.

	Degree of Freedom	Deviation Square Sum	Mean Deviation Squares Sum	F Ratio
A: Sputtering power/(W)	3	114.688	38.229	12.481
B: Sputtering pressure/(Pa)	3	1.688	0.563	0.184
C: Gas flow ratio	3	51.188	17.063	5.571
D: Substrate temperature/(°C)	3	38.688	12.896	4.21
Error	3	9.19	3.063	

2.3.2. Analysis of Process Parameters for Al₂O₃ Film

From Figure 3, we can observe the change trend of alumina film deposition rate with the change of process parameters. From Figure 3a–e, the range of deposition rate is 0.9~7 (nm/min) when the Ar:O₂ flow ratio and sputtering power are constant. The deposition rate of the film increases first and then decreases with the sputtering pressure gradual increasing. The range of deposition rate is 2~13.3 (nm/min) when the Ar:O₂ flow ratio and the sputtering pressure are held constant. The deposition rate of the film increases with the increase of power. The range of deposition rate is 19.1–33.2 (nm/min) when the power and sputtering pressure are constant. The deposition rate of the films increases with the increase of Ar:O₂ flow ratio. This shows that Ar:O₂ flow ratio has the greatest influence and the sputtering pressure has the least influence on the deposition rate.

2.3.3. Analysis of Process Parameters for TiN Films

The deposition rate and surface roughness values of the prepared TiN film are shown in Tables 11 and 12.

Table 11. Effect of process parameters on film deposition rate of TiN film.

		Deposition Rate (nm/min)					
		Negative Bias (V)					
		100	80	60	40	20	0
Ar:N ₂	60:1	66.1	61.1	60.2	59.7	58.4	56.4
	40:1	46.9	42.3	41.8	40.7	39.5	38.6
	30:1	33	34.3	35.6	37.4	35.7	33.5
	25:1	25.7	29.7	31.3	35.3	34.5	31.3
	20:1	21.9	25.6	28.5	31.3	32.8	29.3

Table 12. Effect of process parameters on surface roughness Ra of TiN film.

		Surface Roughness (nm)					
		Negative Bias (V)					
		100	80	60	40	20	0
Ar:N ₂	60:1	27	31	35	39	43	47
	40:1	25	27	31	33	39	43
	30:1	39	34	27	29	31	35
	25:1	31	27	19	21	24	30
	20:1	29	21	15	20	22	27

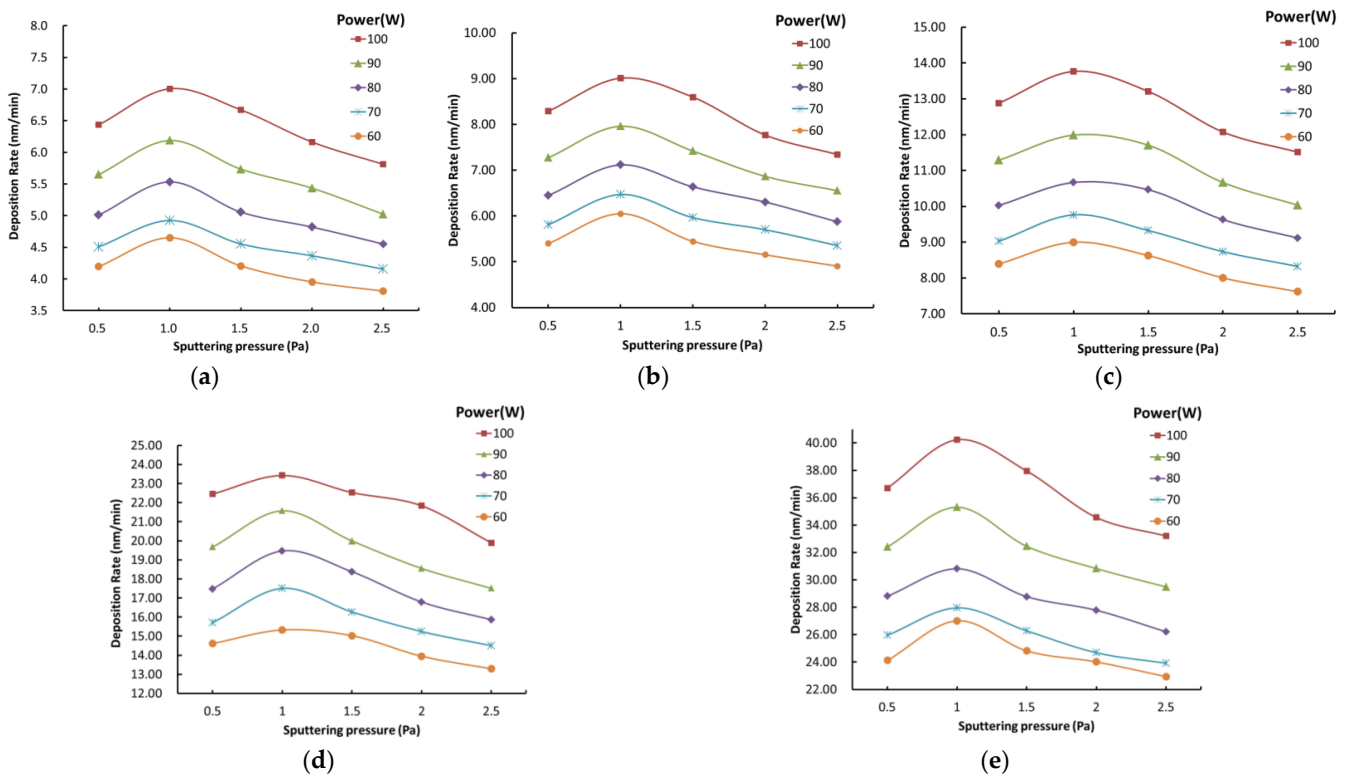


Figure 3. The influence of process parameters on the deposition rate of Al₂O₃ film. (a) Ar:O₂ = 10:1; (b) Ar:O₂ = 20:1; (c) Ar:O₂ = 30:1; (d) Ar:O₂ = 40:1; (e) Ar:O₂ = 50:1.

From Table 11, it can be seen that the deposition rate decreases as the Ar:N₂ flow ratio decreases. The decrease rate changes from 66.1 to 21.9 with the Ar:N₂ flow ratio changes from 60:1 to 20:1 when the substrate negative bias is 100 V. The decrease rate always change from big to small with the Ar:N₂ flow ratio changing from 60:1 to 20:1 under the same substrate negative bias. It can be seen that the deposition rate decrease with the reduction of total gas.

The decrease rate change from 66.1 to 56.4 with the substrate negative bias changing from 100 to 0 when the Ar:N₂ flow ratio is 60:1. The decrease rate increases first and then decreases with the substrate negative bias changing from 100 to 0 when the Ar:N₂ flow ratio is 30:1 or 25:1 or 20:1. When the total gas reduces, the influence of negative bias on the deposition rate increases, then the deposition rate increases with the decrease of substrate negative bias and the deposition rate would decrease when the substrate negative bias disappears. That is, the deposition rate would decrease when the substrate negative bias is large. As a result, it can be seen that the effect of Ar:N₂ flow ratio on deposition rate is greater than substrate negative bias.

From Table 12, the substrate negative bias increases from 0 V to 100 V, the maximum difference of surface roughness is 20 (Ar:N₂ flow ratio is 60:1) and the minimum difference is 12 (Ar:N₂ flow ratio is 20:1) when Ar:N₂ flow ratio is constant. It can be seen that the surface quality is good when Ar:N₂ flow ratio is smaller. When the substrate negative bias of the substrate is constant, the difference of surface roughness is the range of 13–20 nm, and the surface roughness decreases with the decrease of Ar:N₂ flow ratio, but the surface roughness value is irregular when the substrate negative bias is 100 V. It can be seen that in order to obtain better surface quality, a lower substrate negative bias and gas flow ratio are required.

2.3.4. Analysis of Orthogonal Test of Process Parameters for Ni-Cr Film

The data of Table 6 are collected with range analysis, where the range values of the effects of sputtering power, sputtering pressure, negative bias and substrate temperature on deposition rate are 18.62, 0.71, 5.62 and 0.50, respectively. As a result, the influence degree of the process parameters on deposition rate can be obtained as follows: sputtering power > substrate negative bias > sputtering pressure > substrate temperature.

It can be seen from Table 6 that the deposition rate increases gradually with the increase of sputtering power and substrate negative bias. The velocity of the sputtering particles bombarding the substrate increases with the increase of sputtering power, which increases the deposition rate of the film. However, with the increase of the deposition rate, particle energy would increase. As a result, particle energy would affect the surface flatness of films. As the strain sensitive layer in the sensor, the roughness and flatness of the Ni-Cr film are very important for the theoretical calculation of resistance and the accurate measurement of strain. Therefore, the flatness of the film should be ensured while the deposition rate increases.

2.3.5. Analysis of Orthogonal Test of Etching Process Parameters for Ni-Cr Film

The influence of various factors on the film etching rate and the film surface roughness is discussed with the range analysis method according to the results of the orthogonal experimental. As shown in Table 13, where K_i ($i = 1, 2, 3$) is the average of measurement results at each level, and R_j ($j = A, B, C$) is the range of each factor, and where X is incident angle, Y is argon flow, Z is substrate negative bias.

Table 13. Range analysis of thin-film etching experiment results.

	Film Etching Rate $v/(nm/min)$			Film Roughness $Ra/(nm)$			Resistivity $\rho (\mu\Omega \cdot m)$		
	X	Y	Z	X	Y	Z	X	Y	Z
K_1	25.4	23.7	20.3	38.0	34.3	31.7	1.49	1.26	1.14
K_2	24.5	24.8	24.9	30.7	34.3	35.0	1.12	1.33	1.33
K_3	24.6	26.2	29.4	35.0	35.0	37.0	1.31	1.31	1.44
R_j	0.9	2.5	9.1	7.3	0.7	5.3	0.37	0.06	0.30
	Influence level $Z > Y > X$			Influence level $X > Z > Y$			Influence level $X > Z > Y$		

Figure 4 shows the relationship of etching rate, roughness and parameters.

Figure 4a is the range analysis of the process parameters on the film etching rate, the degree of influence: substrate negative bias > argon flow > incident angle. In the etch process, the substrate negative bias and arc voltage are superimposed to form ion source energy. As the energy of the ion beam increases, the energy of the particles transferred to the substrate increases and the material removal speed accelerates and the etching rate increases. Figure 4b shows the range analysis of the process parameters on the film roughness, and the degree of their influence: incident angle > substrate negative bias > argon flow. The Ni-Cr alloy film roughness is important for the protective layer on it, because it is related to the adhesion between the two films. The roughness value is smaller when the incidence angle is 45°.

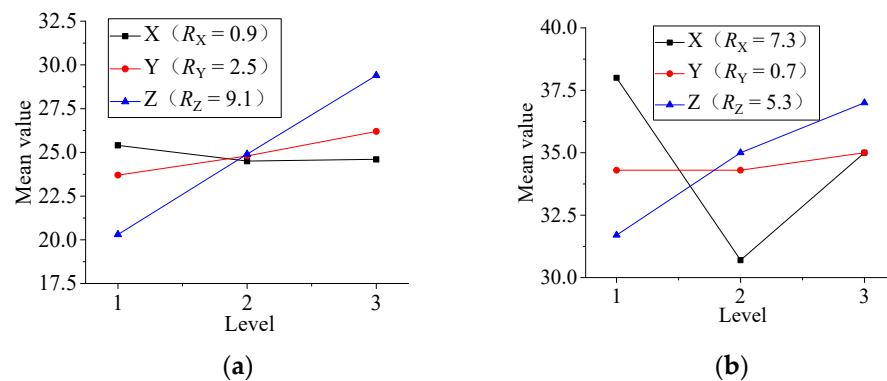


Figure 4. The relationship of etching rate, roughness and parameters. (a) Parameter range analysis of film etching rate; (b) Parameter range analysis of film roughness.

3. Performance Characterizations of Sensors

3.1. Characterization of Microscopic Morphology and Mechanical Properties of Thin-Films

3.1.1. 3-D Morphology of Aluminum Oxide and TiN Transition Layer

Figure 5 shows the 3-D morphology of silicon nitride film, silicon nitride film containing alumina transition layer and silicon nitride film containing titanium nitride transition layer. It can be seen that the average surface roughness of silicon nitride film without transition layer is between 18–33 nm; the average roughness surface of silicon nitride film with alumina film as transition layer is between 17–25 nm, the number of peaks and valleys on significantly less, the surface morphology is relatively smooth; the average roughness surface of silicon nitride film with titanium nitride film as transition layer is between 11–12 nm, the number of peaks and valleys on significantly least, the surface morphology is more smooth. Insulation film quality is especially important for the manufacture of resistance grid layer.

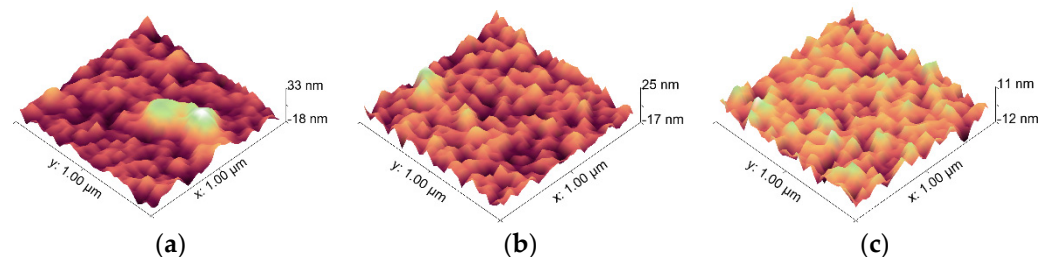


Figure 5. 3-D morphology of silicon nitride thin-film by atomic force microscopy (MFP-3D). (a) Silicon nitride thin-film; (b) Silicon nitride film with Aluminum oxide transition layer; (c) Silicon nitride film with TiN transition layer.

3.1.2. Mechanical Properties of Ni-Cr alloy Resistance Grid Layer

Ni-Cr alloy film has the largest elastic modulus, nano-hardness and resistivity. Aluminum oxide and silicon nitride thin-films were sputtered on 304 stainless steel substrates before sputtering the Ni-Cr alloy films. Then the Ni-Cr alloy films were deposited on the surface of the silicon nitride thin-films. The data are recorded in Figure 6, respectively.

From Figure 6, the elastic modulus Ni-Cr alloy film first increases and then decreases with the increase of sputtering pressure, and then stabilizes. It increases with the increase of sputtering power and substrate negative bias. Therefore, in order to increase the elastic modulus of Ni Cr alloy film, the sputtering power and substrate negative bias can be appropriately increased. The elastic modulus Ni-Cr alloy film has small influence on of when the substrate temperature is below 200 $^{\circ}\text{C}$. The value of the elastic modulus increases from 1F81 to 198 when the temperature is from 200 $^{\circ}\text{C}$ to 300 $^{\circ}\text{C}$. It can be seen that nano hardness of the film are not affected by the change of sputtering pressure, and decrease with sputtering power and substrate temperature. Nanohardness changes periodically with substrate negative bias. The nanohardness mainly changes in the range of 8.3–8.6 GPa.

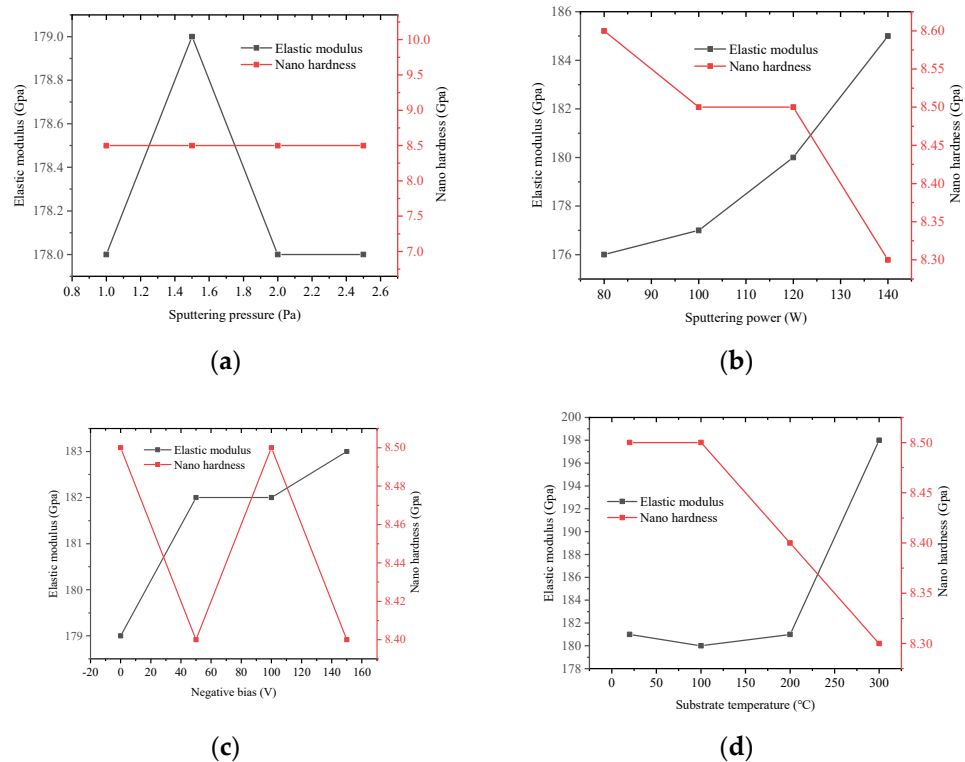


Figure 6. Effect of different process parameters on elastic modulus and nano-hardness. (a) Sputtering pressure curve; (b) Sputtering power curve; (c) Substrate negative bias curve; (d) Substrate temperature curve.

The strain sensitivity coefficient of Ni-Cr alloy film is the most important index to measure the mechanical properties of the film sensor. The larger the coefficient value, the better the sensitivity of the film sensor. Figure 7 shows the values of the strain sensitivity coefficient varying with the elastic modulus. The values of the strain sensitivity coefficients are 1.78, 1.76, 1.74 and 1.56 with elastic modulus of 176, 180, 185 and 198 GPa, respectively. The coefficient value decreases with the increase of elastic modulus.

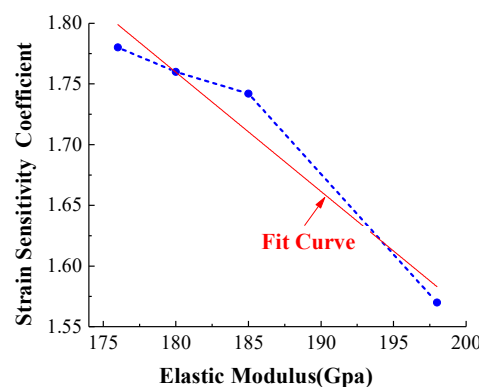


Figure 7. Test results of strain sensitivity coefficient.

Combined with the conclusion of Figure 6, it is necessary for elastic modulus to be a lower value in order to obtain a higher sensitivity coefficient (≥ 1.7). Since the strain sensitivity coefficient of 1.78 corresponds to the elastic modulus of 176 GPa, the corresponding process parameters can be selected according to the requirements of elastic modulus. For example, the sputtering pressure is between 2–2.6 Pa, the sputtering power is less than 110 W, the negative bias voltage of the substrate is less than 20 V, and the substrate temperature is less than 200 °C.

3.2. Characterization of Electrical Properties of Ni-Cr Films with Metal Sensitive Layers

3.2.1. Effect of Geometric Structure Parameters of Resistance Gate on Resistance Strain Coefficient

Through the calculation of the geometric parameters of the resistance grid, the theoretical resistance value of resistance grid is 1200 Ω. The effect of thin-film sensor with different lengths, width and thickness (as shown in Figure 2) on the resistance and resistance strain coefficients is studied. The dimensions are shown in Table 14.

Table 14. Geometrical dimensions of thin-film sensor with different length of resistance grid.

Sample	Longitudinal Resistance Grid Length	Resistance Value: 1200 Ω; Longitudinal Resistance Grid Width: 0.1 mm; Longitudinal Resistance Grid Thickness: 800 nm			Electrode
		Lateral Resistance	Longitudinal Resistance	Single Resistance Grid Resistance Value (Ω)	
1	3 mm	0.4 × 0.4 mm	28	41.25	2 × 2 mm
2	4 mm		21	55	
3	5 mm		17	68.75	
4	6 mm		14	82.5	

The resistance strain coefficients of the prepared thin-film sensor are analyzed by strain measurement, and the load range of 0–400 N is selected for the stretch test. Figure 8 shows the results of the stretch test of the thin-film sensor with resistance grid length, width and thickness under the condition of single factor. It can be seen that the width of the resistance grid has a relatively large influence on the resistance strain coefficient, of which the width of the 0.1 mm has the largest effect. When the strain is less than 300 με, the resistance strain coefficients of different lengths or thicknesses are almost the same. When the strain exceeds 300 με, the resistance strain coefficients of different lengths or thicknesses are slightly different, but there is little difference between the values. The results show that the structure size of the resistance grid has little effect on the resistance strain coefficient.

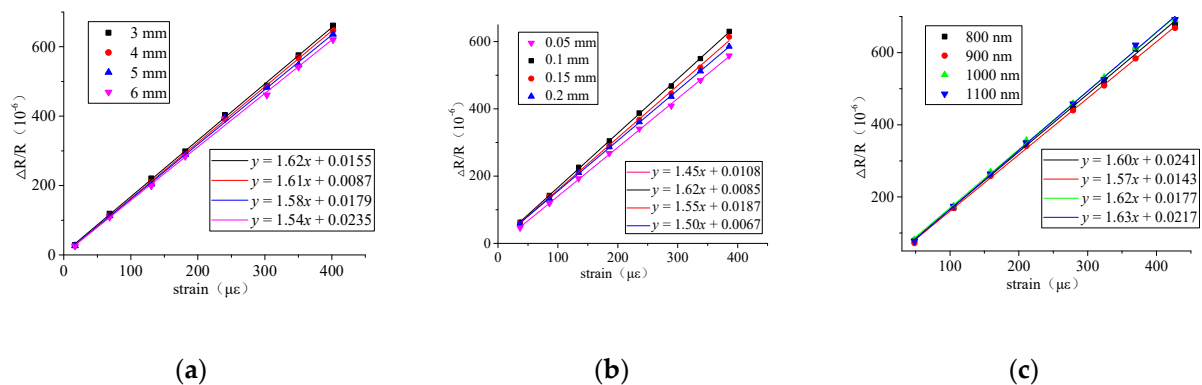


Figure 8. Tensile test results of structure parameters of resistor gratings prepared by etching method. (a) Effect of resistance grid length on resistance strain coefficient; (b) Effect of resistance grid width on resistance strain coefficient; (c) Effect of resistance grid thickness on resistance strain coefficient.

3.2.2. Effect of Etching Parameters on Resistivity

The range analysis is performed for the film etching resistivity test results in Table 13. Figure 9 is the parameter range analysis of surface roughness, it can be seen the degree of influence: incidence angle > substrate negative bias > argon flow. With the increase of incidence angle, the film resistance first increases and then decreases, and the inflection point appears at 45°. It can be seen that the resistivity is the lowest at 45°. In order to obtain high resistivity, the influencing order and level factors of process parameters can be adjusted as needed.

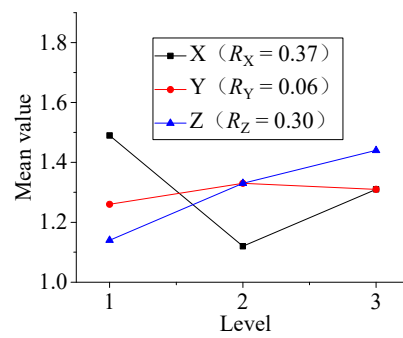


Figure 9. Parameter range analysis of film resistivity.

4. Calibration of Sensor Strain Coefficient

In the experiment of calibrating, unidirectional force is applied to the thin-film strain sensor by tensile tester. There is experiment device in Figure 10a, using a DH5929 dynamic signal test and analysis system to collect strain values of 16 thin film resistor grids that form four groups of Wheatstone bridges, as shown in Figure 10b. The experimental data are shown in Figure 10d, the curve of strain value and output voltage, getting the relationship as Equation (1):

$$U_{out} = \frac{1}{2}k_n \epsilon_n U_{in} \tag{1}$$

where U_{out} is the output voltage of the circuit, k_n is the strain sensitivity coefficient of the thin-film resistance gate, ϵ_n is the strain value of the thin-film resistance gate, and U_{in} is the input voltage of the circuit.

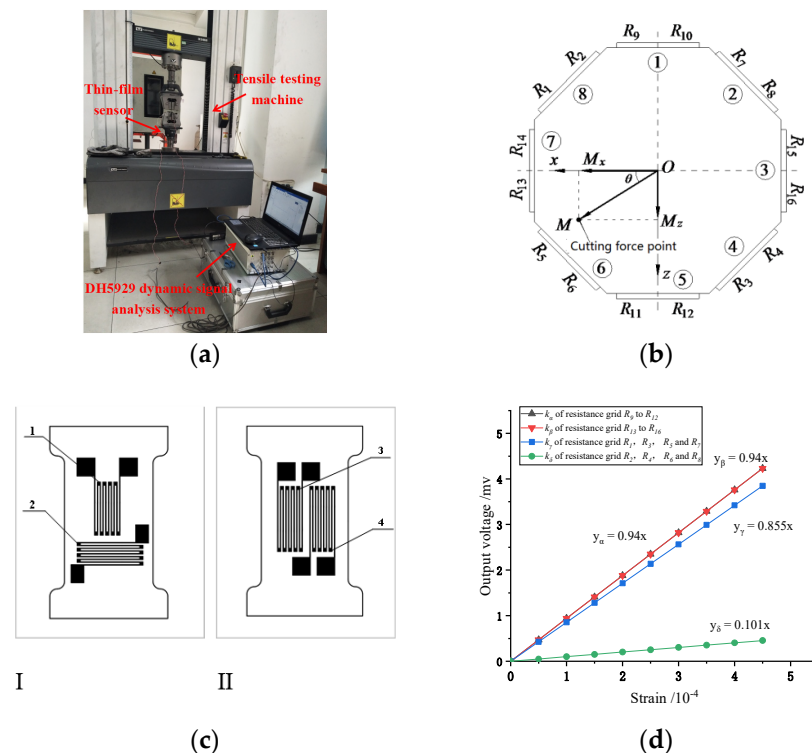


Figure 10. Tensile test of thin film strain sensor. (a) stretching device; (b) Distribution diagram of resistance grid; (c) Resistor grids I and II; (d) Output voltage and strain diagram of thin-film sensor.

The arrangement of 16 resistance grids is shown in Figure 10b. There are four resistor grids arranged on the two resistor grids I and II, as shown in Figure 10c. Resistance grids R₁–R₈ adopts strain gauge I, which is 45 degrees from the horizontal. On the strain gauge I, resistance grids R₁, R₃, R₅ and R₇ adopt the grid 1 which is the longitudinal arrangement,

R_2 , R_4 , R_6 and R_8 adopt the grid 2 which is the horizontal arrangement. Resistance grids R_9 – R_{16} adopt the grid 3 and 4 on the strain gauge II, in which resistance grids 3 and 4 are the longitudinal arrangement. It can be seen from Figure 10d that good linearity exists between strain and electrical signal, which is conducive to the accurate measurement of cutting force. In the Wheatstone bridge circuit, the curve slope between the output voltage and the thin film sensor is 0.5 kn. The equation in Figure 10d, the resistance strain coefficients k_α , k_β , k_γ and k_δ of the thin-film resistance grid are 1.88, 1.88, 1.71 and 0.26 respectively. The resistance strain coefficients k_α and k_β are equal, because resistance grids R_9 – R_{16} are longitudinal arrangement. Resistance grids R_9 – R_{16} are in the same stress state during the tensile test. Resistance strain coefficients k_γ is 1.71 less than 1.88 because resistance grid R_1 , R_3 , R_5 and R_7 are the longitudinal arrangement and 45 degrees from the horizontal. It is in accordance with the resistance strain coefficients of Ni-Cr film between 1~2. Resistance strain coefficients k_δ is 0.26 because resistance grid R_2 , R_4 , R_6 and R_8 are the horizontal arrangement and 45 degrees from the horizontal. In order to obtain the maximum strain, the length direction of the resistance grid needs to be consistent with the load direction, thus obtain a larger output voltage and achieve the purpose of measuring the cutting force.

5. Conclusions

5.1. Effect of Process Parameters on Each Film

The influence degree of the process parameters on the deposition rate of the Si_3N_4 insulating layer is followed by sputtering power, gas flow ratio, substrate temperature, and sputtering pressure. The Ar: O_2 flow ratio has more influence on the deposition rate of Al_2O_3 film than sputtering power and sputtering pressure. The influence degree of the parameters of the deposition rate of the TiN transition layer is followed by Ar: N_2 flow ratio, and substrate negative bias. The substrate negative bias has a greater effect on the surface roughness than Ar: N_2 flow ratio.

The influence degree of process parameters on the deposition rate of Ni-Cr alloy film is followed by sputtering power, substrate negative bias, sputtering pressure, substrate temperature. The influence degree of the etching process parameters on the etching rate of Ni-Cr alloy film is followed by the substrate negative bias, argon flow, and the incident angle, and the order of the influence on the surface roughness is the incident angle, substrate negative bias, and the argon flow. As a result, the film with good performance can be obtained by adjusting the parameters that have a great impact on the film performance.

5.2. Effect of Process Parameters on Each Film

Al_2O_3 and TiN as the transition layer between 304 stainless steel substrate and Si_3N_4 insulating layer can reduce the protrusion on the film surface and improve the surface flatness and uniformity of the Si_3N_4 insulating layer. As a result, it is necessary to increase the transition layer between 304 stainless steel substrate and Si_3N_4 insulating layer in order to improve the performance of insulating layer

5.3. Effect of Process Parameters on Each Film

For the Ni-Cr alloy film, the elastic modulus of the Ni-Cr alloy film is inversely proportional to sputtering power, directly proportional to substrate negative bias and sputtering pressure. When the substrate temperature is less than 200 °C, the elastic modulus of the film has little effect. The Nano-hardness of the films is inversely proportional to the sputtering pressure and substrate temperature, and varies periodically under the substrate negative bias of 0–160 V.

5.4. Effect of Process Parameters on Each Film

Greater strain can be obtained when the length direction of the resistance grid consistent with the load direction, thus obtain a larger output voltage and achieve the purpose of measuring the cutting force. Thin film strain sensors can be selectively placed according to different cutting conditions.

Author Contributions: Conceptualization, W.W. and Y.C.; methodology, W.W. and Y.C.; experiments, Y.C. and Y.Z.; software, L.L.; validation, Z.H.; formal analysis, D.S.; resources, W.W. and Y.C.; data curation, Y.C.; writing—original draft preparation, Y.C.; reviewed and edited the paper, W.W. All authors have read and agreed to the published version of the manuscript.

Funding: This work was supported by the National Natural Science Foundation of China (51875533); Shanxi Provincial Natural Science Foundation of China (201901D111130; 201901D111179).

Conflicts of Interest: The authors declare no conflict of interest.

References

1. Kuntoğlu, M.; Aslan, A.; Pimenov, D.Y.; Giasin, K.; Mikolajczyk, T.; Sharma, S. Modeling of cutting parameters and tool geometry for multi-criteria optimization of surface roughness and vibration via response surface methodology in turning of AISI 5140 steel. *Materials* **2020**, *13*, 4242.
2. Kuntoğlu, M.; Aslan, A.; Pimenov, D.Y.; Usca, Ü.A.; Salur, E.; Gupta, M.K.; Mikolajczyk, T.; Giasin, K.; Kapłonek, W.; Sharma, S. A review of indirect tool condition monitoring systems and decision-making methods in turning: Critical analysis and trends. *Sensors* **2021**, *21*, 108. [[CrossRef](#)] [[PubMed](#)]
3. Kuntoğlu, M.; Acar, O.; Gupta, M.K.; Sağlam, H.; Sarikaya, M.; Giasin, K.; Pimenov, D. Parametric optimization for cutting forces and material removal rate in the turning of AISI 5140. *Machines* **2021**, *9*, 90. [[CrossRef](#)]
4. Kuntoğlu, M.; Aslan, A.; Sağlam, H.; Pimenov, D.Y.; Giasin, K.; Mikolajczyk, T. Optimization and analysis of surface roughness, flank wear and 5 different sensorial data via tool condition monitoring system in turning of AISI 5140. *Sensors* **2020**, *20*, 4377. [[CrossRef](#)] [[PubMed](#)]
5. Kiswanto, G.; Putri, S.K.; Fitriawan, M.R.; Hiltansyah, F.; Putra, R.G. Modeling, Simulation, and Analysis of Cutting Force in Micro End Milling Process of Mild Steel Using Mechanistic Model. In Proceedings of the 2021 7th International Conference on Mechatronics and Robotics Engineering (ICMRE), Budapest, Hungary, 3–5 February 2021.
6. Yıldız, S.; Ünsaçar, F. Design, development and testing of a turning dynamometer for cutting force measurement. *Mater. Des.* **2006**, *27*, 839–846. [[CrossRef](#)]
7. Castro, L.R.; PViéville Lipinski, P. Correction of dynamic effects on force measurements made with piezoelectric dynamometers. *Int. J. Mach. Tools Manuf.* **2006**, *46*, 1707–1715. [[CrossRef](#)]
8. Yıldız, S.; Unsacar, F.; Sağlam, H.; Işık, H. Design, development and testing of a four-component milling dynamometer for the measurement of cutting force and torque. *Mech. Syst. Signal Process.* **2007**, *21*, 1499–1511. [[CrossRef](#)]
9. Sağlam, H.; Unuvar, A. Three-Component, Strain Gage Based Milling Dynamometer Design and Manufacturing. *J. Integr. Des. Process Sci.* **2001**, *5*, 95–109.
10. Zhao, Y.; Zhao, Y.; Ge, X. The Development of a Triaxial Cutting Force Sensor Based on a MEMS Strain Gauge. *Micromachines* **2018**, *9*, 30. [[CrossRef](#)]
11. Zhang, X.Y.; Lu, X.; Wang, S.; Wang, W.; Li, W.D. A multi-sensor based online tool condition monitoring system for milling process. *Procedia CIRP* **2018**, *72*, 1136–1141. [[CrossRef](#)]
12. Zhang, H.; Li, Z.; He, W.; Ma, C.; Liao, B.; Li, Y. Mechanical modification and damage mechanism evolution of TiN films subjected to cyclic nano-impact by adjusting N/Ti ratios. *J. Alloy. Compd.* **2019**, *809*, 151816. [[CrossRef](#)]
13. Chen, Q.; Li, A.; Wu, G.; Lu, Z.; Zhang, G.; Tian, G. Structure vs chemistry: Tribological behavior of TiN films in the nitrogen atmosphere. *Ceram. Int.* **2020**, *46*, 28053–28063. [[CrossRef](#)]
14. Chou, W.J.; Yu, G.P.; Huang, J.H. Mechanical properties of TiN thin-film coatings on 304 stainless steel substrates. *Surf. Coat. Technol.* **2002**, *149*, 7–13. [[CrossRef](#)]
15. Qi, R.; Pan, L.; Feng, Y.; Wu, J.; Li, W.; Wang, Z. Evolution of chemical, structural, and mechanical properties of titanium nitride thin-films deposited under different nitrogen partial pressure. *Results Phys.* **2020**, *19*, 103416. [[CrossRef](#)]
16. Kumar, P.K.; Manikandan, V.N.; Raj, P.D.; Sridharan, M. Characterization of magnetron sputtered Si₃N₄ thin-films deposited on Aluminum alloy substrates. *Mater. Today Proc.* **2016**, *3*, 1536–1540. [[CrossRef](#)]
17. Nemanič, V.; McGuinness, P.J.; Daneu, N.; Zajec, B.; Siketić, Z.; Waldhauser, W. Hydrogen permeation through silicon nitride films. *J. Alloy. Compd.* **2012**, *539*, 184–189. [[CrossRef](#)]
18. Batan, A.; Franquet, A.; Vereecken, J.; Reniers, F. Characterisation of the silicon nitride thin-films deposited by plasma magnetron. *Surf. Interface Anal. Int. J. Devoted Dev. Appl. Tech. Anal. Surf. Interfaces Thin-Film.* **2008**, *40*, 754–757. [[CrossRef](#)]
19. Yao, Z.Q.; Yang, P.; Huang, N.; Wang, J.; Wen, F.; Leng, Y.X. Studies of the composition, tribology and wetting behavior of silicon nitride films formed by pulsed reactive closed-field unbalanced magnetron sputtering. *Nucl. Instrum. Methods Phys. Res. Sect. B Beam Interact. Mater. At.* **2006**, *242*, 33–36. [[CrossRef](#)]
20. Petley, V.; Sathishkumar, S.; Raman, K.T.; Rao, G.M.; Chandrasekhar, U. Microstructural and mechanical characteristics of Ni–Cr thin-films. *Mater. Res. Bull.* **2015**, *66*, 59–64. [[CrossRef](#)]
21. Lai, L.; Fu, X.; Sun, R.; Du, R. Comparison of microstructure and electrical properties of Ni–Cr alloy thin-film deposited on different substrates. *Surf. Coat. Technol.* **2013**, *235*, 552–560. [[CrossRef](#)]
22. Lai, L.; Zeng, W.; Fu, X.; Sun, R.; Du, R. Optimization of sputtering parameters for Ni–Cr alloy deposition on copper foil as embedded thin-film resistor. *Surf. Coat. Technol.* **2013**, *218*, 80–86. [[CrossRef](#)]

23. Zhang, Y.; Wu, W.; Han, Y.; Wu, X.; Cheng, Y.; Liu, L. Adhesion analysis of silicon nitride film deposited on stainless steel surface by adding transition layer. *Nanotechnology* **2020**, *31*, 215711. [[CrossRef](#)] [[PubMed](#)]
24. Zhang, Y.; Wu, W.; Han, Y.; Wen, H.; Cheng, Y.; Liu, L. Design and Analysis of a Turning Dynamometer Embedded in Thin-Film Sensor. *Micromachines* **2019**, *10*, 210. [[CrossRef](#)] [[PubMed](#)]
25. Li, X.; Wu, W.; Cheng, Y.; Liu, L. Structure design and optimization for a cutting force measurement tool with embedded nickel–chromium film sensor. *Adv. Mech. Eng.* **2018**, *10*, 168781401875988. [[CrossRef](#)]
26. Cheng, Y.P.; Wu, W.G.; Du, X.J.; Qiao, G.L. Design and Analysis of Constantan Thin Films Sensor for Monitoring Cutting Force. *Appl. Mech. Mater.* **2014**, *635–637*, 882–885. [[CrossRef](#)]
27. Cheng, Y.P.; Wu, W.G.; Li, X.R.; Du, X.J. Design and Theoretical Analysis of An Embedded Thin Film Sensor. *Mater. Sci. Forum* **2014**, *800*, 788–792. [[CrossRef](#)]
28. Ma, R.; Wu, W.; He, Z.; Cheng, Y.; Liu, L.; Zhao, Y. Construction and Characterization of TiN/Si₃N₄ Composite Insulation Layer in TiN/Si₃N₄/Ni₈₀Cr₂₀ Thin Film Cutting Force Sensor. *Micromachines* **2021**, *12*, 1476. [[CrossRef](#)]
29. Cheng, Y.; Wu, W.; Liu, L.; He, Z.; Song, D. Structural design and optimization of a turning tool embedded with thin-film strain sensors for in-process cutting force measurement. *AIP Adv.* **2022**, *12*, 015126. [[CrossRef](#)]
30. Abaci, S.; Nessark, B. Characterization and corrosion protection properties of composite material (PANI+TiO₂) coatings on A304 stainless steel. *J. Coat. Technol. Res.* **2015**, *12*, 107–120. [[CrossRef](#)]
31. Escarraga, A.; Toro, A.; Aguilar, Y.; Caicedo, J.C.; Zambrano, G. Thermal cyclic response of [8YSZ/Al₂O₃] n multilayered coatings deposited onto AISI 304 stainless steel. *Mater. Chem. Phys.* **2018**, *216*, 526–533. [[CrossRef](#)]
32. Saravanan, M.; Devaraju, A.; Venkateshwaran, N.; Krishnakumari, A.; Saarvesh, J. A review on recent progress in coatings on AISI austenitic stainless steel—Science Direct. *Mater. Today Proc.* **2018**, *5*, 14392–14396. [[CrossRef](#)]